

Preliminary Measurements of Time-Resolved Ion Velocity Distributions Near a Hollow Cathode

IEPC-2015-106/ISTS-2015-b-106

*Presented at Joint Conference of 30th International Symposium on Space Technology and Science,
34th International Electric Propulsion Conference and 6th Nano-satellite Symposium
Hyogo-Kobe, Japan
July 4–10, 2015*

Marcel Georgin*, Christopher Durot† and Alec D. Gallimore‡
University of Michigan, Ann Arbor, Michigan, 48109, USA

Presented are preliminary measurements of near-cathode ion velocity distributions using time-resolved laser induced fluorescence. Two experiments were performed. First, time-averaged velocity distributions were measured in a LaB₆ hollow cathode plume under the influence of a Hall thruster magnetic field provided by the 6-kW H6 thruster. The discharge was sustained without a downstream anode but rather using the cathode's heater and keeper. Time-averaged velocity distributions were measured at several axial positions downstream from the cathode. Additionally, the ion velocity distribution was measured at the cathode exit without the magnetic field. The second experiment measured time-resolved ion velocity distributions. Operating the cathode in a similar manner, the measurements were made at the cathode exit under nominal and high magnetic field conditions. Lastly, a time-resolved velocity distribution was measured at the cathode exit in the full Hall thruster discharge under nominal magnetic field conditions.

Nomenclature

\mathbf{B}	= magnetic field
\mathbf{B}^*	= nominal magnetic field
d	= scale length
f_{mod}	= time-resolved modulation frequency
\bar{f}_{mod}	= time-averaged modulation frequency
k_B	= Boltzmann's constant
m_{Xe}	= mass of xenon
T	= temperature
v	= ion velocity
v_i	= initial ion velocity
v_0	= mean velocity
z_i	= initial position
z_f	= final position
α	= Maxwellian fit parameter

*Ph.D. Student, Applied Physics, georginm@umich.edu

†Ph.D. Student, Applied Physics, durot@umich.edu

‡Arthur F. Thurnau Professor, Aerospace Engineering, alec.gallimore@umich.edu

I. Introduction

WHILE Hall thruster technology has matured significantly, a full physical understanding of how these devices operate does not exist. What was initially called a stationary plasma thruster is in fact highly oscillatory and these oscillations have been shown to impact performance.¹ Two primary thruster oscillation modes are present in Hall thruster discharges. They are typically referred to as the global and local modes. The global mode oscillations exhibit a strong “breathing” characteristic of the entire channel, oscillating between 5 – 20 kHz.^{1–4} The local mode oscillations can be described as rotating spokes which oscillate between 5 – 60 kHz.^{1,3,5,6} Plasma oscillations are also present in the hollow cathode discharge and are typically observed in the 40 – 90-kHz range.^{7,8} Further understanding of the effect these oscillations have on performance and long-term thruster operation is necessary. Hall thrusters have been shown to change their oscillatory mode with magnetic field strength.¹ When a thruster is in a magnetically shielded configuration, the oscillations observed in the discharge are at a higher frequency, in the range of 40 – 90 kHz which suggests a stronger coupling to the cathode that also exhibits oscillations in the 40 – 90-kHz range.^{1,7}

Laser induced fluorescence (LIF) is a spectroscopic technique that measures the ion velocity. Atoms and ions have well-defined electronic transitions which can be excited using a laser. If the ions are moving, the laser wavelength observed by the ions will be Doppler shifted. When measuring a velocity distribution, the wavelength of the laser is swept around the electronic transition energy. Using the equation for the Doppler shifting of light, each wavelength can be mapped to an ion velocity. At any given wavelength, the laser will only excite ions whose velocity correctly Doppler shifts the laser’s wavelength to the electronic transition energy. The ion velocity distribution can then be constructed measuring the light fluoresced by the ions at different wavelengths. Time-averaged velocity distributions both in Hall thrusters and hollow cathodes have been well characterized,^{9–11} however these measurements ignore the time dependence of plasma properties and valuable information is lost. A time-resolved diagnostic is required to better understand how plasma oscillations affect performance and lifetime.

Making time-resolved LIF measurements in Hall thrusters is challenging, not only because the fluorescence signal is weak, but also because of the chaotic nature of the oscillations. Classical LIF uses a lock-in amplifier to recover the fluorescence; however, due to the poor signal to noise ratio, the integration time, τ , must typically be set to 100 ms or more¹² to acquire a velocity distribution. Since oscillations in Hall thrusters are between 10 – 100 kHz,¹³ this technique cannot provide the time resolution needed to observe oscillations in the velocity distribution. One approach to time-resolved LIF is to use the lock-in amplifier with a short time constant and to average over a time-series with an oscilloscope set to trigger at the beginning of the laser pulse.¹² Since Hall thruster plasmas don’t necessarily have repeatable triggers, this averaging process dephases and the signal ultimately decays with time.

A novel time-resolved LIF system was developed by Durot¹² in the Plasmadynamics and Electric Propulsion Laboratory (PEPL) at the University of Michigan. This technique uses a transfer function averaging method that assumes that the thruster acts as a linear system whose input is the discharge current, I_D , and the outputs are plasma properties such as the ion velocity, v , or ion density. This technique was first used for high-speed Langmuir probe analysis by Lobbia.¹⁴ The advantage this method has over the typical triggered average method is that it operates in frequency space. Since a full spectrum in Fourier space is taken at each data point, the unphysical decay caused by varying oscillation periods is avoided.¹² A detailed explanation of this LIF technique is available in Ref. 12.

This work examines the time-averaged and time-resolved ion velocity distributions in the cathode plume to begin to characterize coupling between the cathode and thruster. The primary motivation behind this work is to improve the understanding of the cathode’s impact on thruster lifetime. Magnetic shielding has minimized channel erosion making cathode and magnetic pole erosion the next likely failure modes. A deeper understanding of the erosion mechanisms will help facilitate future thruster design to mitigate cathode and pole erosion. Additionally, the observation of increased cathode-channel coupling in magnetically shielded Hall thrusters poses the question: how do cathode oscillations impact thruster performance? This work is a preliminary step to answering these questions.

II. Experimental Setup

The following sections describe the experimental setup for the time-averaged and time-resolved LIF measurements. The experiments were conducted at PEPL in the Large Vacuum Test Facility (LVTF).

LVTF is a cylindrical vacuum chamber which is 9 m long and 6 m in diameter. The chamber used four mechanical pumps to achieve a rough vacuum, then seven cryogenic pumps to attain a base pressure of 5×10^{-7} Torr which is measured by an ion gauge mounted behind the thruster.

A. External Setup

For a xenon plasma, the transition to a metastable state $5d[4]_{7/2} \rightarrow 6p[3]_{5/2}^o$ was probed with a Toptica TA Pro continuous wave laser. The wavelength associated with this transition is $\lambda = 834.724$ nm in air while the fluorescence signal is collected at 541.9 nm. The Toptica TA Pro diode laser typically outputs 200 mW and has a mode-hop free range of 20 – 50 GHz. To verify the stability and performance of the laser, the beam was sampled by an etalon (Fabry-Pérot interferometer), wavemeter, optogalvanic cell (a low pressure Xe gas discharge), and a photodiode. The etalon was used to verify that the laser was in a single mode while the wavemeter monitors the wavelength. The optogalvanic cell was used as a wavelength reference for the xenon transition and the photodiode measured the laser's output power. After the beam was sampled, it was focused and sent into the acousto-optic modulator (AOM). The AOM was used as a high-frequency chopper to modulate the signal. For the time-averaged measurement, the AOM was modulated at $f_{mod} = 98$ kHz and for the time-resolved experiment it was modulated at $f_{mod} = 1$ MHz. The beam was then collimated and sent into the chamber. A diagram of the external setup verifying the beam's performance is shown in the upper part of Fig. 1.

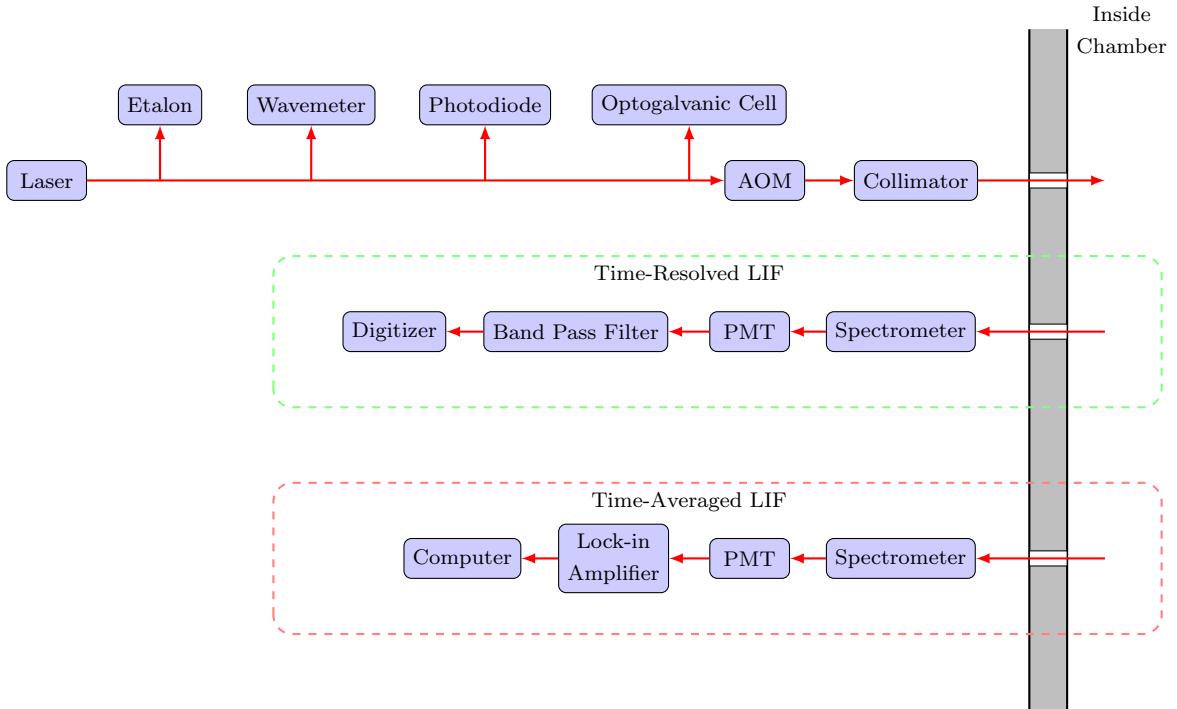


Figure 1: External optical setup. Top most are the measurement devices used to verify the operation of the laser. Circled in green is the time-resolved LIF signal processing path. Circled in red is the time-averaged signal processing path.

After the fluorescence signal was captured by the collection optics inside the chamber, it was sent out via fiber optic cable for post processing. Two processing paths were available. The first procedure was for the time-averaged LIF measurement (circled in red in Fig. 1) and the second was for the time-resolved experiment (circled in green in Fig. 1). For time-averaged LIF, the fluorescence signal was sent into a spectrometer that was set to pass the xenon fluorescence wavelength at 541.9 ± 1 nm. This signal was sent to the photo-multiplier to produce an electronic signal and then passed to a lock-in amplifier with a time constant of $\tau = 100$ ms. The measurement was recorded by a computer via a custom LabView interface.

Similarly, for the time-resolved measurement the LIF signal was first sent into the spectrometer. Then, a photomultiplier tube converts and amplifies the optical signal to an electronic signal that was then filtered

with a band pass filter that was set to allow frequencies: $f_{mod} \pm 10\%$. This was then recorded by an Alazartech digitizer at 30 MHz for 60 s. The laser's wavelength was then swept to interrogate ions with different velocities and to build the velocity distribution. The discharge current and the floating potential were measured since they can be used as the input signal to the transfer function analysis technique. The discharge current measurements were made with a high-speed current probe. The floating potential was measured with a floating probe placed 5 mean thruster channel diameters downstream. These signals were digitized using another Alazartech card at 30-MHz.

B. Internal Setup

An illustration of the internal setup is shown in Fig. 2. Once the collimated beam was sent through the chamber wall, it was passed to the injection optics via a fiber optic cable. The beam was sent through a polarizer and then focused on the exit plane of the thruster. The injection optics were controlled by a pair of servo motors that rotated the optics in the polar and azimuthal directions. This portion of the setup was protected from the ion beam by a grafoil shield. The fluorescence was then captured by the collection optics. The collection lens was 76 mm in diameter and has a focal length of about 130 mm. The signal was sent out of the chamber through a fiber optic cable. The polar and azimuthal orientations of the collection were similarly controlled via two servo motors. The collection stand and optics were protected by a grafoil shield. A floating potential probe was placed five thruster diameters downstream from the exit plane of the thruster on a motion stage that gave a range of ± 0.5 thruster diameters.

Two plasma sources were used during these experiments; one was a LaB₆ cathode and the other was the 6-kW H6 Hall thruster. The thruster was attached to the x - z motion stages via a leveling plate. The motion stages were used to move the thruster, permitting the apparatus to change the point of interrogation in the cathode or thruster discharge.

The laser alignment procedure first aligned the injection optics to the motion stages. Then the thruster was aligned with the injection to ensure that the axial component of the ion velocity, v_z , was sampled and to maintain perpendicularity when moving the thruster. Lastly, the collection was aligned to the injection at the exit plane of the thruster using a reflective pin. While testing, the stages were periodically moved to verify that alignment was maintained during the experiment.

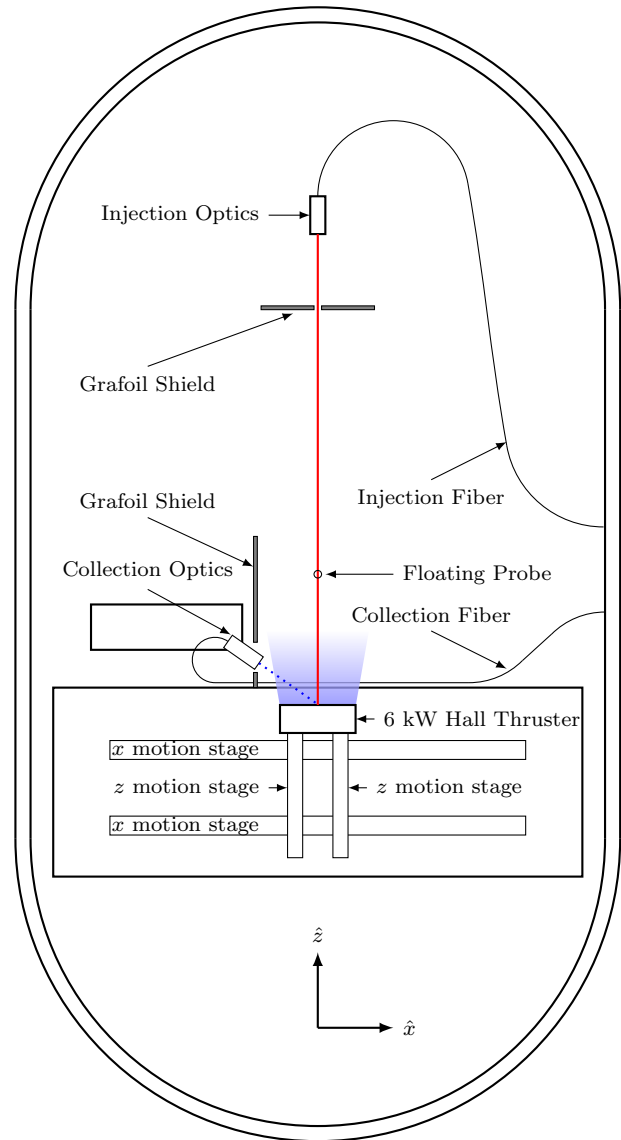


Figure 2: The setup inside LVTF for time-resolved LIF measurements in a 6-kW Hall thruster. The axial direction is \hat{z} , the azimuthal angle, ϕ , is in the $x-z$ plane, and the polar angle, θ , is measured from the vertical axis \hat{y} (not shown). This image is not to scale.

C. Operation of the Plasma Sources

Typically, when experiments are conducted on hollow cathodes, the cathode is operated independently of the thruster and a positively biased anode is placed downstream. The anode helps stabilize the cathode discharge. In this work, the cathode was operated without a downstream anode, using the heater and keeper to stabilize the discharge.

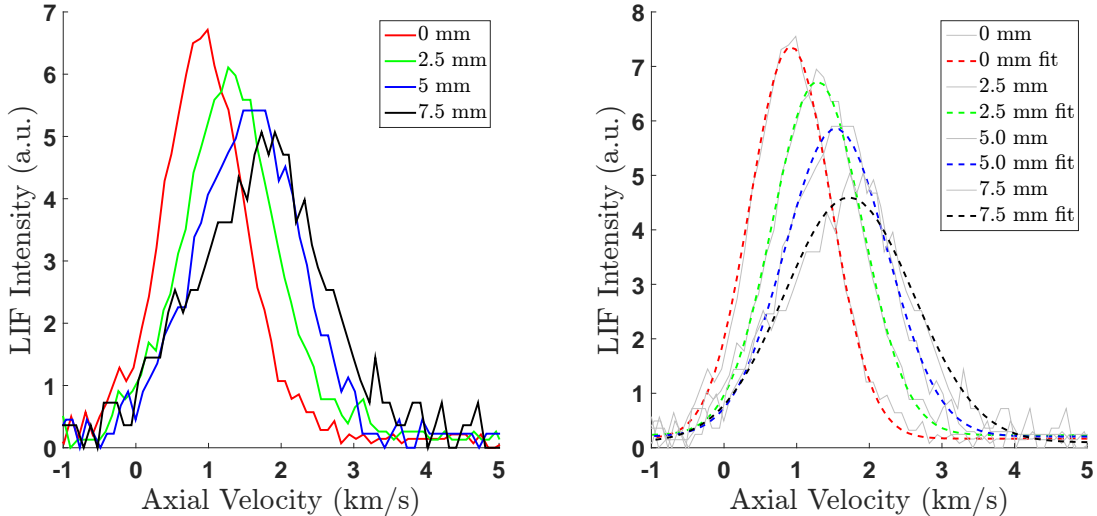
In these experiments, the cathode was brought to a steady discharge using the following procedure. The Hall thruster was first lit and brought to a steady state under nominal magnetic field conditions. The discharge voltage was 150 V with a propellant flow rate of 10 mg/s with a 10% cathode flow fraction. Once the cathode-to-ground voltage stabilized (around -9 V), the cathode heater was turned to between 3 and 5 A and the keeper was biased to 24 V above the cathode, requiring about 3.5 A. Then the potential on the thruster anode and the thruster propellant flow were removed. After allowing the cathode-to-ground voltage to re-stabilize (between -2 and -3 V), the magnetic field was adjusted to its final condition and the LIF measurements were started. The magnetic field conditions tested were the nominal field ($\mathbf{B} = \mathbf{B}^*$), a high-field case ($\mathbf{B} = 1.5 \mathbf{B}^*$), and no field ($\mathbf{B} = 0$).

For the thruster measurements, the Hall thruster anode was biased to 150 V while flowing 10 mg/s of xenon propellant with a 10% cathode flow fraction. Thruster power was at 1.5-kW and the magnetic field was set to the nominal condition.

III. Results & Discussion

A. Time-Averaged Experiment

1. Axial Position Sweep



(a) Time averaged axial ion-velocity distribution measured at several axial positions. The distributions are integral normalized.

(b) One dimensional Maxwellian curve fits to the time-averaged axial ion-velocity distribution measured at several axial positions.

Figure 3: Comparison of the axial ion-velocity distribution at positions downstream from the cathode at the nominal field condition.

The first time-averaged experiment was the axial position sweep of the LaB_6 cathode plume. The recorded axial ion-velocity distributions are presented in Fig. 3a. Figure 3a shows that the axial velocity increases while the distribution broadens with distance downstream from the cathode. To understand this quantitatively,

these ion velocity distributions were fit with one-dimensional Maxwellian velocity distributions:

$$p(v) = \sqrt{\frac{\alpha}{\pi}} e^{-\alpha(v-v_0)^2} + c \quad (1)$$

where $\alpha = \frac{mX_e}{2k_B T}$, v_0 is the peak velocity, and c is an offset due to background noise. Generally, it is expected that $c \approx 0$. The fits are shown in Fig. 3b and the fit parameters are displayed in Table 1. Table 1 shows that α decreases with distance, implying that the ions are getting hotter since $\alpha \propto \frac{1}{T}$. Additionally, the values of v_0 indicate that the average axial velocity is increasing with distance. This is expected since the keeper is biased positively and should be repelling the ions from the cathode towards the grounded chamber walls. The ‘‘goodness’’ of these fits was determined using the χ^2 goodness-of-fit criterion. The uncertainty in the fluorescence was estimated by looking at parts of the fluorescence trace without a signal and taking the standard deviation of the noise. The uncertainty in the velocity was computed by propagating the uncertainty in the wavelength. The reduced χ^2 for these fits were between 0.6 and 2.3, which indicates that this model fits the data well and that the plasma is roughly Maxwellian.

Table 1: Results from the one dimensional Maxwellian distribution fit to the data in Fig. 3a using Eqn. (1).

	α (m/s) ⁻²	v_0 (km/s)	c
0 mm	1.63×10^{-6}	0.917	1.67×10^{-5}
2.5 mm	1.33×10^{-6}	1.284	2.31×10^{-5}
5 mm	1.00×10^{-6}	1.540	2.05×10^{-5}
7.5 mm	0.64×10^{-6}	1.681	1.10×10^{-5}

Using the parameter α , the ion temperature can be estimated assuming other peak broadening mechanisms are negligible. Since $\alpha = \frac{mX_e}{2k_B T}$, the ion temperature as a function of position downstream can be calculated. The results of this analysis are shown in Fig. 4. The estimated ion temperatures are increasing as a function of distance from about 0.4 eV to approximately 1 eV. The uncertainties shown in Fig. 4 are the propagated statistical uncertainty based on the fit parameters. These results can be considered as an upper-bound on the ion temperature. The increase in ion temperature could be indicative of collisions in the near-cathode plume.

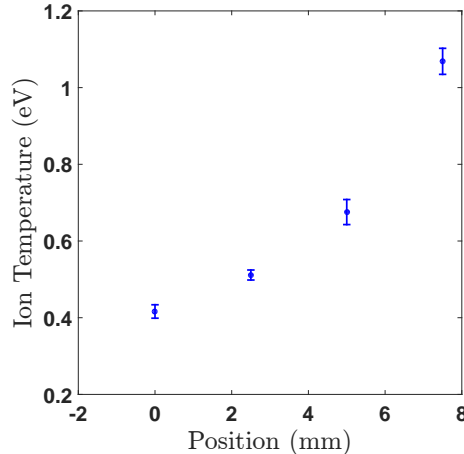


Figure 4: Estimated ion temperatures calculated from the width of the fluorescence spectrum. The uncertainties shown are the statistical uncertainties derived from the fit parameters.

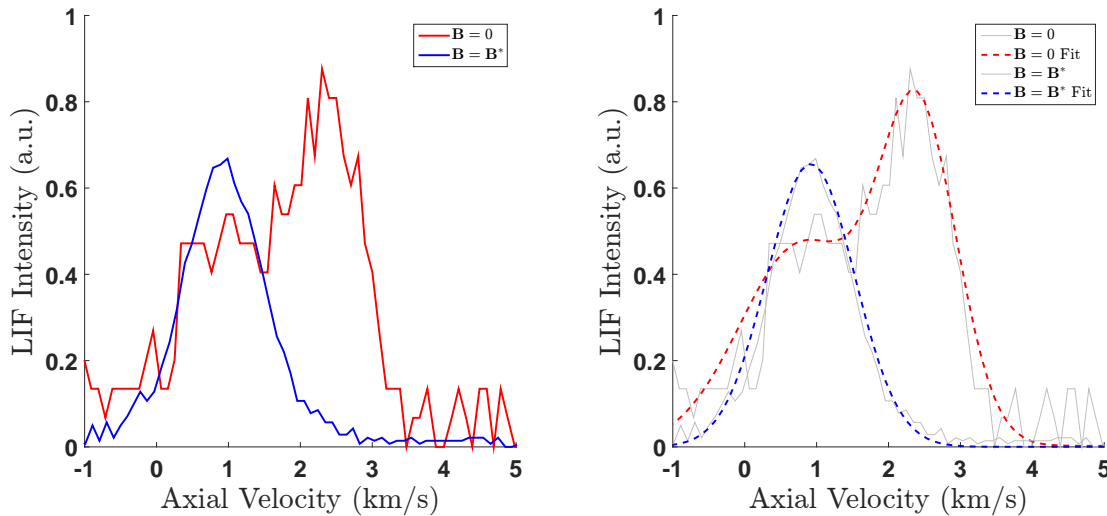
2. $B = B^*$ and $B = 0$ Comparison

For the next test condition, the magnetic field was removed and a time-averaged velocity distribution was measured. Figure 5a shows the integral-normalized velocity distribution functions. Under the no-field condition (in red), a double distribution is observed in the axial velocity distribution which is described by:

$$p(v) = \sqrt{\frac{\alpha}{\pi}} e^{-\alpha(v-v_0)^2} + \sqrt{\frac{\alpha_2}{\pi}} e^{-\alpha_2(v-v_{0_2})^2} + c \quad (2)$$

The fit parameters are shown in Table 2. Again, the χ^2 goodness-of-fit test concludes that there is relatively good agreement between the model and the data. The reduced $\chi^2 = 2.5$ is slightly high, however this is expected since the no-field distribution is noisy. Both distributions show velocity peaks in the 800 – 900 m/s range. The mean of these peaks are statistically different (3σ), however they are still within each other’s half-width half-maximum. Therefore it is likely that they are the same peak. It is possible that remnants of the thruster’s magnetic field persisted, causing the axial ion-velocity to have a similar peak. This measurement was repeated to confirm the presence of the low velocity peak. Further investigation on this subject is required to determine if this peak is due to a remnant magnetic field or actual plasmadynamics.

The difference between the main no-field peak and the nominal field peak is about 1.5 km/s. Visibly, the thruster’s magnetic field appears to improve the stability of the cathode discharge. These ion velocity distribution measurements indicate that either ions are slowed by the magnetic field, or they are rotated such that the axial components of their velocity is reduced. Electrons near the cathode are magnetized, however ions should be non-magnetized.



(a) Time averaged axial ion-velocity distribution measured at two field conditions. The red distribution is with $B = 0$ and the blue is with $B = B^*$. The distributions are integral normalized.

(b) The red distribution is the double Maxwellian fit to the $B = 0$ velocity distribution, the blue is the single Maxwellian fit with $B = B^*$.

Figure 5: Comparison of cathode operation under nominal magnetic field and with no magnetic field.

B. Time-Resolved Experiment

The time-resolved experiments looked at the cathode discharge under nominal and high magnetic field conditions without a thruster discharge as well as a near-cathode measurement while operating the thruster. The high-field condition was $B = 1.5 B^*$. All the measurements reported in this section were made at the

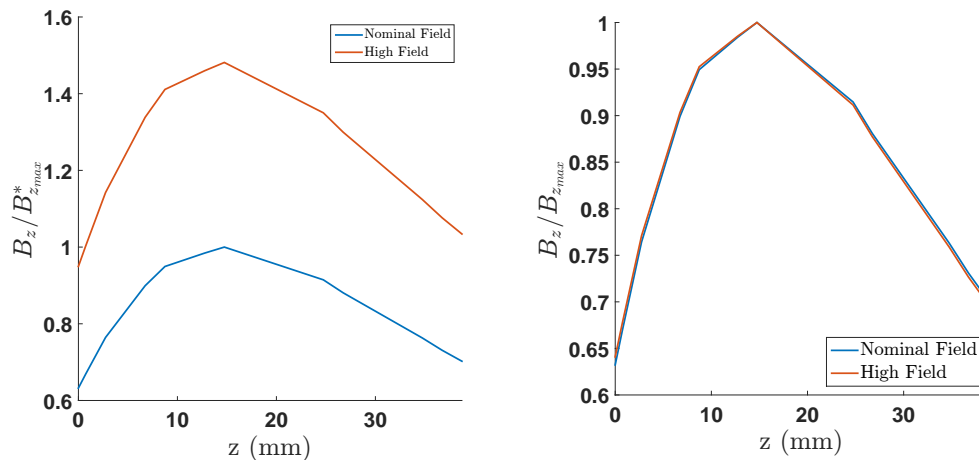
Table 2: Fit parameters for the magnetic field test using Eqn. (1) for $\mathbf{B} = \mathbf{B}^*$ and Eqn. (2) for $\mathbf{B} = 0$.

	α (m/s) ⁻²	v_0 (km/s)	c	α_2 (m/s) ⁻²	v_{0_2} (km/s)
$\mathbf{B} = 0$	6.88×10^{-7}	0.794	2.37×10^{-6}	1.73×10^{-6}	2.420
$\mathbf{B} = \mathbf{B}^*$	1.63×10^{-6}	0.917	1.67×10^{-5}	–	–

cathode exit plane, at a 10% cathode flow fraction. The keeper was set to 24 V and 3.5 A while the heater current was between 3 and 5 A for the cathode experiments.

1. Magnetic Field Topology

To understand how the magnetic field is being manipulated, simulations using MagNet 7.4 of the cathode centerline magnetic field were conducted. The results are shown in Fig. 6. The change in the field intensity between the two conditions is illustrated in Fig. 6a, while Fig. 6b shows the invariance of the topology of the field and that only the intensity of the field has been changed between the two conditions. The magnetic field near the cathode is primarily axial and is never strong enough to magnetize ions. Note that all the time-averaged measurements were made within the region of increasing magnetic field.



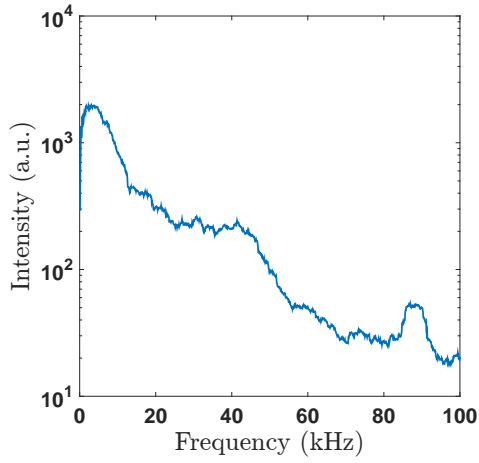
(a) Nominal and high magnetic field normalized by the nominal field maximum. (b) Comparison of the normalized nominal and high magnetic fields.

Figure 6: Comparison of the high and low magnetic field conditions, highlighting that the topology has not changed between the conditions.

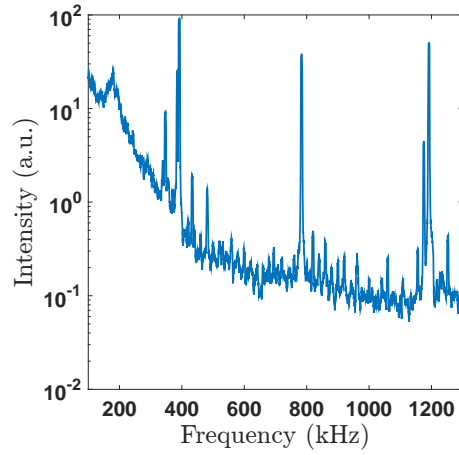
2. Power Spectra

Figure 7 shows the power spectra of the discharge current measurements for each operating condition. The rows in Fig. 7 correspond to the different operating conditions. The first column shows the power spectra for frequencies between 0 and 100 kHz while the second shows the frequency components between 100 and 1300 kHz. Note the difference in scales for both intensity and frequency.

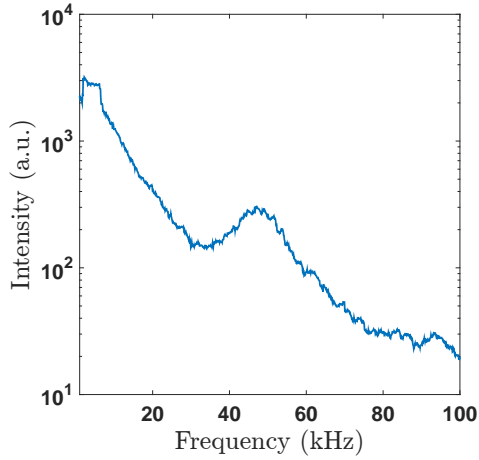
Comparing the images in the first column, a strong 40 to 50-kHz peak was observed in both the cathode conditions (Fig. 7a and Fig. 7c) but was suppressed when the thruster discharge was present (Fig. 7e). Additionally, when the magnetic field was at the nominal condition (Fig. 7a and Fig. 7e), a 90-kHz peak was observed, but this peak was largely suppressed in the high-field condition (Fig. 7c). This result suggests that the magnetic field works to suppress cathode oscillations. When the thruster is on (Fig. 7e), a strong breathing mode was observed at the cathode exit which was not seen when only the cathode was lit (Fig. 7a and Fig. 7c).



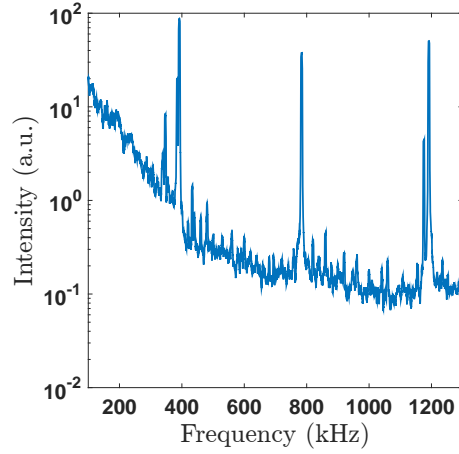
(a) Cathode power spectrum. $B = B^*$



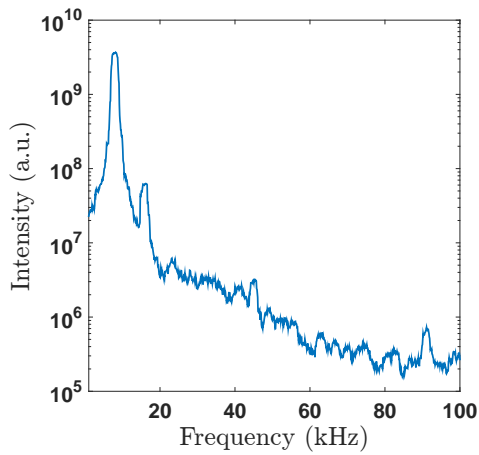
(b) Cathode power spectrum. $B = B^*$



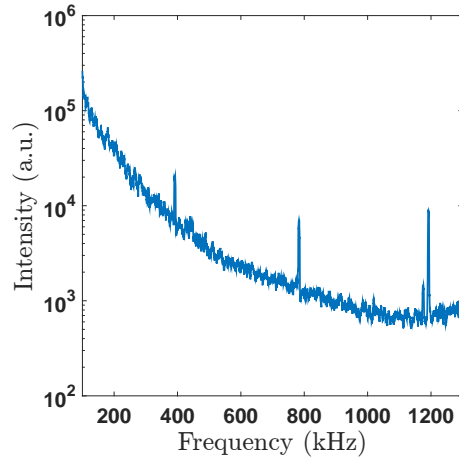
(c) Cathode power spectrum. $B = 1.5 B^*$



(d) Cathode power spectrum. $B = 1.5 B^*$



(e) Near-cathode power spectrum with the thruster on. $B = B^*$



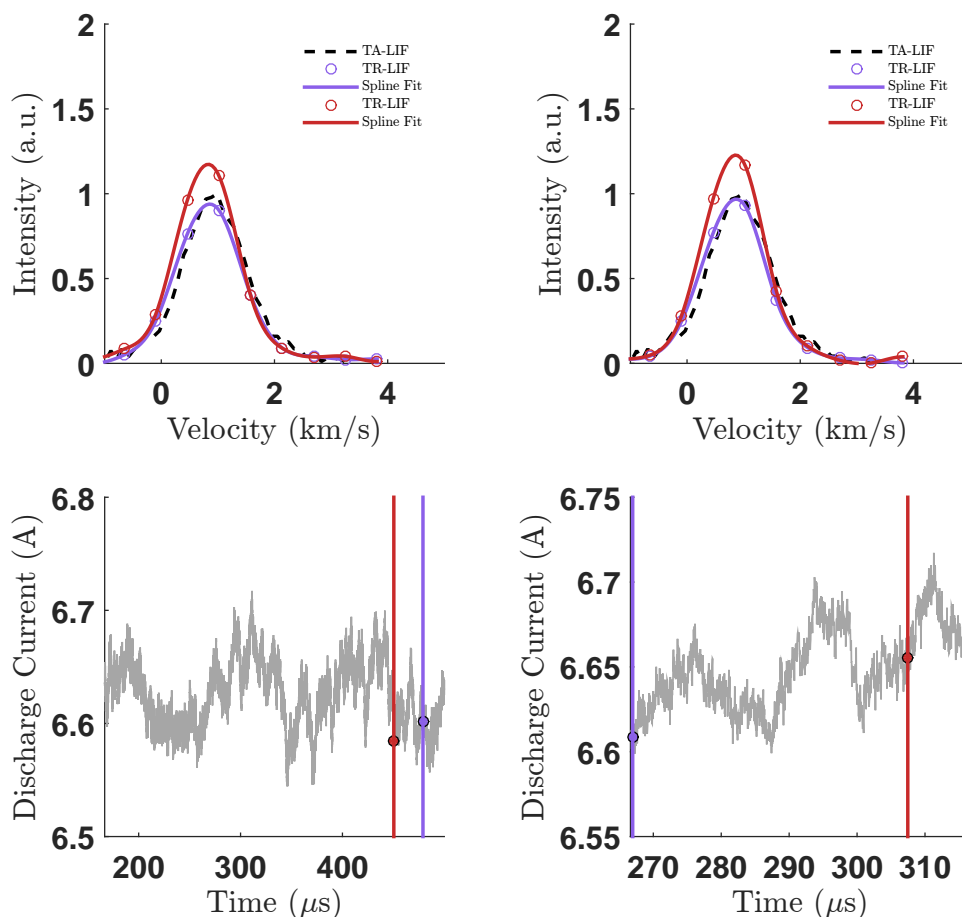
(f) Near-cathode power spectrum with the thruster on. $B = B^*$

Figure 7: Power spectra from the acquired current traces from the time-resolved experiments.

Comparing the power spectral densities in the second column, a 391-kHz oscillation and its harmonics were present in all three power spectra. For the cathode experiments (Fig. 7b and Fig. 7d), these high-frequency peaks had intensities that were on the order of the 40 and 90-kHz oscillations. For the thruster experiment (Fig. 7f), the high-frequency peaks were present but their prominence was diminished by the stronger background signal produced by the thruster. This suggests these peaks don't carry large a fraction of the power compared to the global mode oscillations.

Ultimately, these measurements can be used to determine the time-scales over which interesting phenomena may appear in the time-resolved velocity distributions. To observe a few oscillations around 10 kHz, the time scale should be in the 100's of μs . For the higher frequency oscillations in the 50-kHz range, the time scales should be on the order of 10's of μs .

3. Cathode Measurements



(a) Time-dependent ion velocity distribution for oscillations in the 10-kHz range.

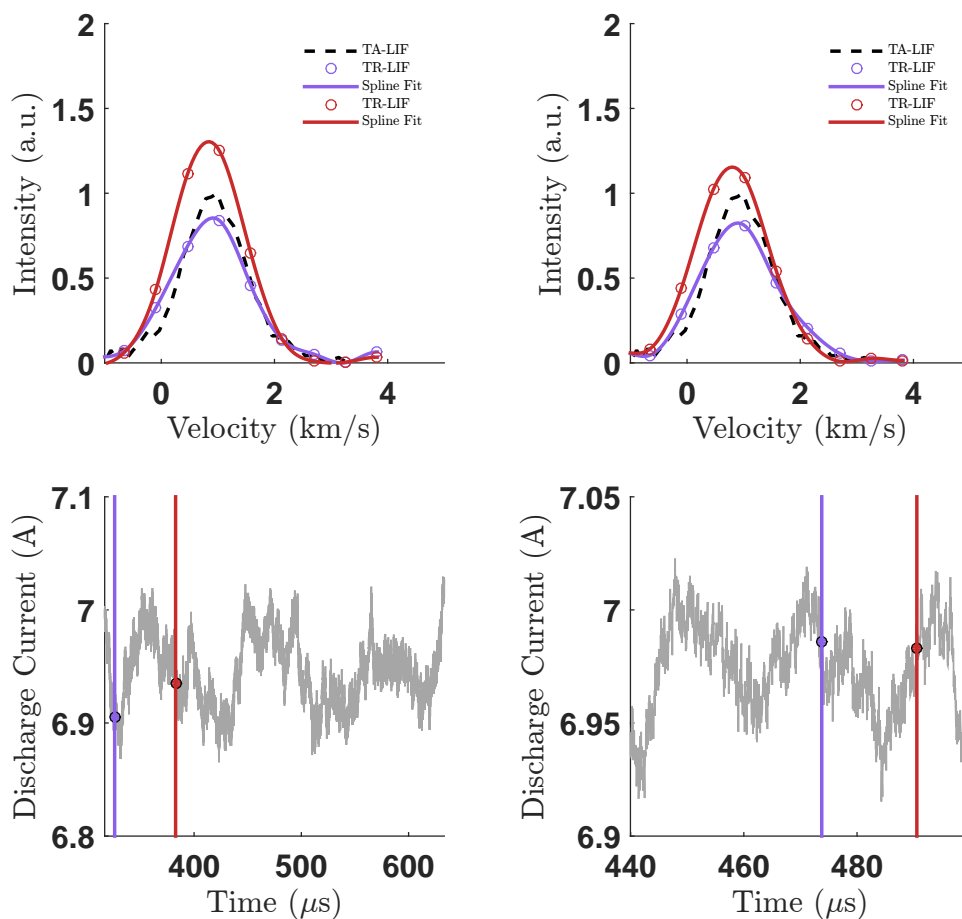
(b) Time-dependent ion velocity distribution for oscillations in the 50-kHz range.

Figure 8: Time-resolved measurements of the ion velocity distribution at cathode orifice during cathode operation at $B = B^*$.

Below, the time-resolved axial ion-velocity distribution is presented and discussed for the nominal and high-field cathode test conditions. Figure 8 contains the discharge current traces and their corresponding velocity distributions under the influence of the thruster's nominal magnetic field. The columns show oscillations over

two time-scales. Figure 8a shows discharge current oscillations at around 10 kHz while Fig. 8b shows current oscillations around 50 kHz. The first row in Fig. 8 shows the time-resolved distribution at two different points in time plotted over the time-averaged measurement. These two points in time were picked to show the typical variation in the amplitude of the fluorescence measurement over the time-scale. The second row shows the discharge current trace which produces the LIF signal.

The first row of Fig. 8a and Fig. 8b shows that the amplitude of the fluorescence oscillations are approximately the same on both time-scales. The peak-to-peak variation is about 0.25 times the average peak intensity. This implies that the fluorescence signal oscillates about its mean with an amplitude that is 12.5% of the mean value. Note that amplitude of the oscillations in the discharge current changed by a factor 0.75 between Fig. 8a and Fig. 8b. Although it is not immediately apparent from Fig. 8, there is a phase shift between the discharge current oscillations and the fluorescence signal. This phase shift is present on both time-scales. A phase relationship is generally expected between the discharge current and the fluorescence signal since it takes time for the effects of the oscillation to manifest themselves in the cathode plume.



(a) Time-dependent ion velocity distribution for oscillations in the 10-kHz range.

(b) Time-dependent ion velocity distribution for oscillations in the 50-kHz range.

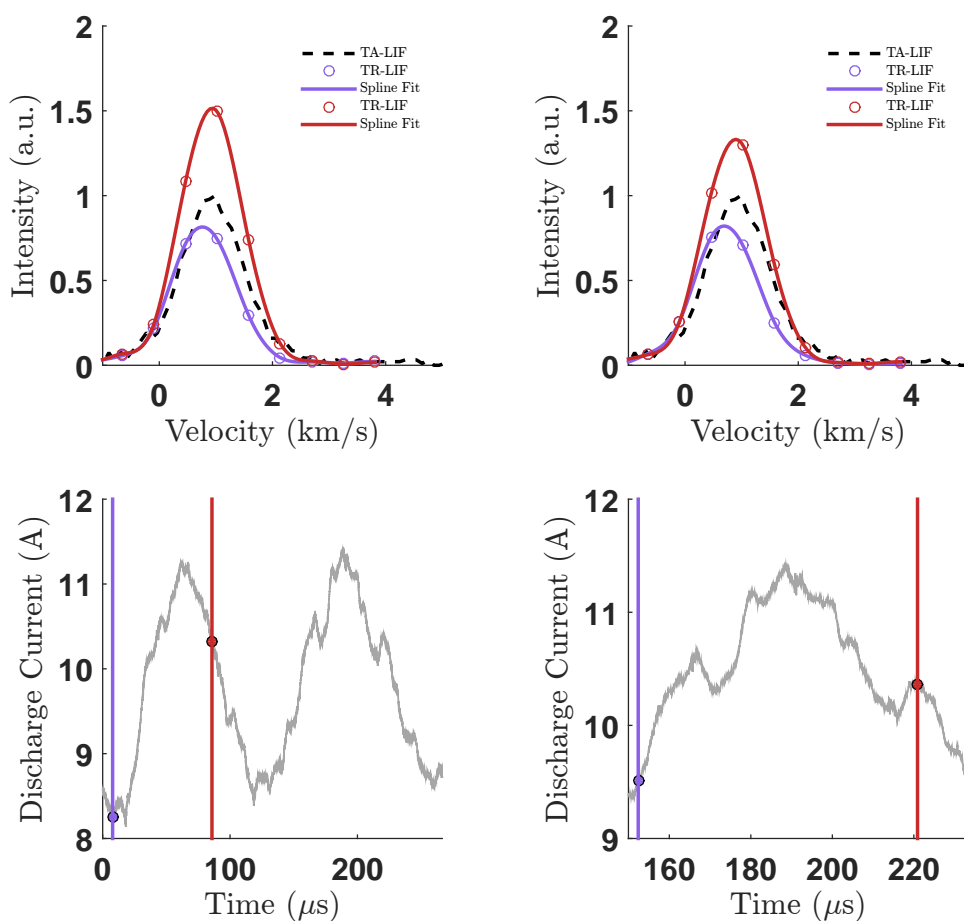
Figure 9: Time-resolved measurements of the ion velocity distribution at cathode orifice during cathode operation at $B = 1.5 B^*$.

Figure 9 shows the time-resolved velocity distributions for the high-field condition and is organized in the same way as Fig. 8. Two points in time were chosen to show the typical oscillation amplitude of the fluorescence signal. Figures 9a and 9b show the fluorescence spectra for discharge current oscillations around

10 kHz and 50 kHz respectively. On the 10-kHz time-scale, peak-to-peak amplitude of the fluorescence signal is roughly 0.5 times the average. For the 50-kHz time-scale, the peak-to-peak amplitude of the fluorescence signal is about 0.4 times the average. The minima in the fluorescence signal for both time-scales are about the same, however, the peak signal is clearly smaller on the 50-kHz scale. Between the two time-scales, the amplitude of the discharge current oscillation has changed by about a factor of 2. Again, a phase shift was observed between the discharge current and fluorescence oscillations and was present on both time-scales.

Comparing the two nominal and high-field test conditions, it is clear that the amplitude of the oscillations increased when the magnetic field was increased. Additionally, when looking at the full time traces (rather than the snapshots shown here), the high-field condition was generally more chaotic than the nominal condition. Typically when observing the cathode plume, applying a magnetic field appears to stabilize the plume and the cathode-to-ground voltage. Based on this, these results are slightly counter-intuitive and require further investigation.

4. Near-Cathode Thruster Measurements



(a) Time-dependent ion velocity distribution for oscillations in the 10-kHz range. (b) Time-dependent ion velocity distribution for oscillations in the 50-kHz range.

Figure 10: Time-resolved measurements of the ion velocity distribution at cathode orifice during thruster operation under nominal magnetic field conditions.

The time-dependent axial ion-velocity distribution during thruster operation is shown in Fig. 10. This figure is organized in the same fashion as Figures 8 and 9. The first row shows the typical oscillation amplitude across that time-scale. The amplitude of the breathing mode, shown in Fig. 10a, is large compared to other oscillatory modes shown in Fig. 10b. This makes it difficult to analyze the higher-frequency modes present in the discharge current signal without filtering the discharge current. Further consideration of analysis techniques for this data is required to build confidence in the interpretations of these results. Nonetheless, these results will be analyzed using the method as for the time-resolved cathode measurements.

In Fig. 10a, approximately 10-kHz oscillations are shown. These are the oscillations typically observed when a thruster is said to be in global oscillation mode. The amplitude of the oscillation is approximately 1.5 times the time average. Figure 10b shows oscillations on the time scales corresponding to the 50-kHz range. These discharge current oscillations induce an oscillation in the velocity distribution whose peak amplitude is about 1.4 times the time average peak. However, this amplitude is convoluted with breathing oscillations, that likely produce the majority of the oscillation in the fluorescence signal.

On average, the velocity distributions shown in Fig. 8 and Fig. 10 are very similar. Other than the oscillations, the thruster discharge does not appear to affect the characteristics of velocity distribution near the cathode on average. This indicates that the anode potential does not couple strongly to ions near the cathode. This result remains unexplained and requires further experiments. A measurement of the plasma potential near the cathode would help understand how the plasma environment is affecting the ion velocity distribution.

5. Comparison of Velocity Distribution Oscillations

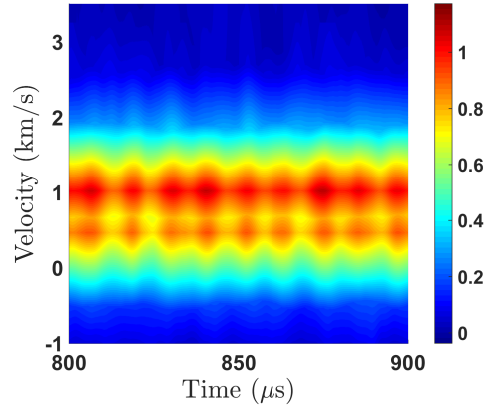
Figure 11 illustrates the evolution of the velocity distributions in time for each of the time-resolved test conditions. Figure 11a is the time-evolution of the cathode velocity distribution for the $\mathbf{B} = \mathbf{B}^*$ magnetic field condition. In Fig. 11a, 90-kHz oscillations were observed in the velocity distribution. These oscillations appeared throughout the trace and were very periodic in time, indicating a quiescent mode of operation for the cathode.

Figure 11b shows the time-evolution of the cathode velocity distribution for the $\mathbf{B} = 1.5\mathbf{B}^*$ magnetic field condition. Figure 11b contains two dominant oscillatory modes. The first is a 90-kHz oscillation which is present throughout the trace and is characterized by a small amplitude oscillation in the fluorescence signal. Additionally, there is a 50-kHz oscillation which is intermittent. The oscillatory mode of this condition can be described as being between two modes, one which exhibits 90-kHz oscillations and another which has oscillations at 50 kHz. The 50-kHz oscillation is the source of the greatest variation in the fluorescence signal for this test condition.

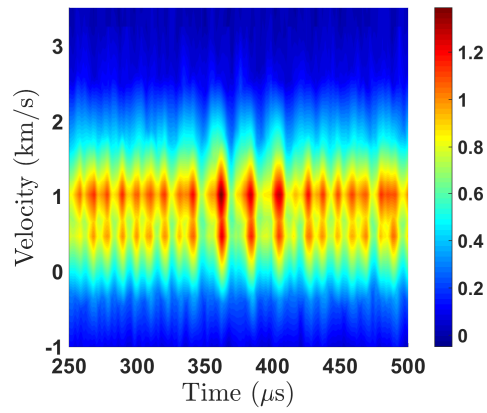
Lastly, Fig. 11c depicts the time-evolution of velocity distribution during thruster operation at the $\mathbf{B} = \mathbf{B}^*$ magnetic field condition. The dominant form of oscillation comes from the thruster breathing mode, however, there is an additional 90-kHz oscillation which comes from the cathode. Although this cathode oscillation is much smaller, its peak-to-peak amplitude is still approximately 15% of the mean.

A first point of comparison is the presence of the 90-kHz cathode oscillation in both of the $\mathbf{B} = \mathbf{B}^*$ conditions. Additionally, they both lack the 50-kHz oscillation from the $\mathbf{B} = 1.5\mathbf{B}^*$ condition. This implies that changing the strength of the magnetic field is changing the oscillatory mode of the velocity distribution.

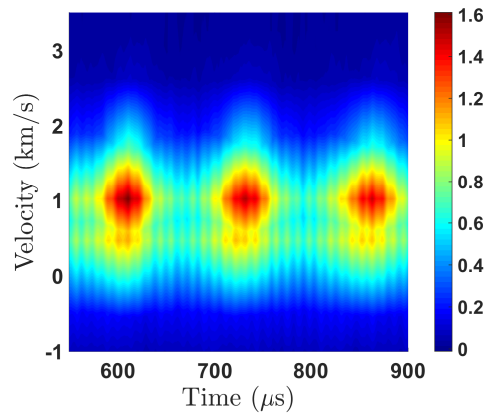
Second, the oscillations present in the velocity distribution can be compared to the oscillations in the discharge current by looking at the power spectra shown in Fig. 7. The primary oscillatory mode in the cathode velocity distribution at $\mathbf{B} = \mathbf{B}^*$ is 90 kHz which corresponds to the 90-kHz peak observed in Fig. 7a. For the $\mathbf{B} = 1.5\mathbf{B}^*$ condition, both the 50 and 90-kHz oscillations are present in the velocity distribution, however in Fig. 7c, the 90-kHz peak is close to the noise of the spectrum. For the thruster measurement, both the breathing mode at about 7 kHz and the cathode oscillation at 90 kHz were present in the velocity distribution. In Fig. 7e, however, only a small peak at 90 kHz is visible in the discharge current which is several orders of magnitude below the breathing mode peak. This implies that even small oscillations in the discharge current can affect the ion velocity distribution.



(a) Cathode velocity distribution in time for the $B = B^*$ condition.



(b) Cathode velocity distribution in time for the $B = 1.5B^*$ condition.



(c) Near-cathode thruster velocity distribution in time for the $B = B^*$ condition.

Figure 11: Velocity distributions in time.

IV. Conclusions

These preliminary results show time-averaged and time-resolved axial ion-velocity distributions near the hollow cathode of a Hall thruster. The time-averaged experiment showed that when the cathode was operated with the keeper-cathode gap for the $\mathbf{B} = \mathbf{B}^*$ condition, ions are accelerated away from the cathode by the potential on the keeper. By removing the magnetic field, a two-population distribution was measured. One peak in the no-field condition matched to the peak with the field on, suggesting the existence of a persisting magnetic field after the current to the inductive coils is shut off.

The time-resolved measurements showed how the velocity distribution at the cathode exit evolves with time. The time-averaged characteristics between cathode measurements and thruster measurements are almost identical suggesting that the coupling of ions near the cathode to the anode is small and perhaps shielded by the thruster discharge. The thruster oscillations, however, do couple to cathode ions.

V. Future Work

To better understand thruster-cathode coupling, the effects of magnetic field strength on cathode oscillations, and the effects of cathode oscillations on erosion, more data is required. First and foremost, the signal to noise ratio must be improved. Next, a more detailed time-averaged axial position sweep will help better understand the cathode environment. Additional time-averaged measurements can include a sweep of the magnetic field to determine the effects of the field strength on the ion velocities. Future time-resolved measurements could include a position sweep to determine the acceleration potential as well as a more complete magnetic field sweep. Measurements off-axis of the cathode could also provide information on cathode and pole erosion. Measurements with a biased downstream or thruster anode will help improve the understanding of the effects of the anode near the cathode. Other signals for the transfer function analysis could include the cathode-to-ground voltage or the keeper voltage and current.

VI. Acknowledgments

The authors would like to thank Dr. Timothy B. Smith for his input on the experimental setup. This work was supported by the Air Force Office of Scientific Research (AFOSR) and the Air Force Research Laboratory (AFRL) through Michigan / Air Force Center of Excellence in Electric Propulsion (MACEEP) Grant No. FA9550-09-1-0695. We would like to thank Dr. Mitat Birkan and Dr. Daniel Brown, the MACEEP program managers from AFOSR and AFRL, respectively.

References

- ¹ Sekerak, M. J., *Plasma oscillations and operational modes in Hall effect thrusters*, Ph.D. thesis, University of Michigan, 2014.
- ² Lobbia, R. B., *A Time-resolved Investigation of the Hall Thruster Breathing Mode*, Ph.D. thesis, University of Michigan, 2010.
- ³ Hara, K., Sekerak, M. J., Boyd, I. D., and Gallimore, A. D., "Mode transition of a Hall thruster discharge plasma," *Journal of Applied Physics*, Vol. 115, No. 20, May 2014.
- ⁴ Fife, J., Martinez-Sanchez, M., Szabo, J., Fife, J., Martinez-Sanchez, M., and Szabo, J., "A numerical study of low-frequency discharge oscillations in Hall thrusters," American Institute of Aeronautics and Astronautics, July 1997.
- ⁵ Sekerak, M. J., Hofer, R. R., Polk, J. E., Longmier, B. W., Gallimore, A., and Brown, D. L., "Mode Transitions in Hall Effect Thrusters," American Institute of Aeronautics and Astronautics, July 2013.
- ⁶ Choueiri, E. Y., "Fundamental difference between the two Hall thruster variants," *Physics of Plasmas (1994-present)*, Vol. 8, No. 11, Nov. 2001, pp. 5025–5033.
- ⁷ Jorns, B. A. and Hofer, R. R., "Plasma oscillations in a 6-kW magnetically shielded Hall thruster," *Physics of Plasmas*, Vol. 21, No. 053512 (2014), May 2014.
- ⁸ Thomas, R. E., Kamhawi, H., and Williams Jr, G. J., "High Current Hollow Cathode Plasma Plume Measurements," 2013.
- ⁹ Williams Jr, G. J., Smith, T. B., Domonkos, M. T., Gallimore, A. D., and Drake, R. P., "Laser-induced fluorescence characterization of ions emitted from hollow cathodes," *Plasma Science, IEEE Transactions on*, Vol. 28, No. 5, 2000, pp. 1664–1675.

- ¹⁰ Huang, W., *Study of Hall thruster discharge channel wall erosion via optical diagnostics*, Ph.D. thesis, University of Michigan, 2011.
- ¹¹ Hargus, W. A. and Charles, C. S., “Near-Plume Laser-Induced Fluorescence Velocity Measurements of a Medium Power Hall Thruster,” *Journal of Propulsion and Power*, Vol. 26, No. 1, Jan. 2010, pp. 135–141.
- ¹² Durot, C. J., Gallimore, A. D., and Smith, T. B., “Validation and evaluation of a novel time-resolved laser-induced fluorescence technique,” *Review of Scientific Instruments*, Vol. 85, No. 1, 2014.
- ¹³ Zhurin, V. V., Kaufman, H. R., and Robinson, R. S., “Physics of closed drift thrusters,” *Plasma Sources Science and Technology*, Vol. 8, No. (1999) R1R20., 1999, pp. R1.
- ¹⁴ Lobbia, R. B. and Gallimore, A. D., “A method of measuring transient plume properties,” *Proceedings of the 44th Joint Propulsion Conference, Hartford, USA, AIAA*, 2008.